

Sensorless adaptive-optics optical coherence tomographic angiography

ACNER CAMINO,¹ PENGXIAO ZANG,¹ ARMAN ATHWAL,² SHUIBIN NI,¹ YALI JIA,^{1,3}  DAVID HUANG,¹ AND YIFAN JIAN^{1,*}

¹Casey Eye Institute, Oregon Health & Science University, Portland, OR 97239, USA

²Department of Engineering Science, Simon Fraser University, Burnaby, Canada

³Department of Biomedical Engineering, Oregon Health & Science University, Portland, OR 97239, USA

*jian@ohsu.edu

Abstract: Optical coherence tomographic angiography (OCTA) can image the retinal blood flow but visualization of the capillary caliber is limited by the low lateral resolution. Adaptive optics (AO) can be used to compensate ocular aberrations when using high numerical aperture (NA), and thus improve image resolution. However, previously reported AO-OCTA instruments were large and complex, and have a small sub-millimeter field of view (FOV) that hinders the extraction of biomarkers with clinical relevance. In this manuscript, we developed a sensorless AO-OCTA prototype with an intermediate numerical aperture to produce depth-resolved angiograms with high resolution and signal-to-noise ratio over a 2×2 mm FOV, with a focal spot diameter of $6 \mu\text{m}$, which is about 3 times finer than typical commercial OCT systems. We believe these parameters may represent a better tradeoff between resolution and FOV compared to large-NA AO systems, since the spot size matches better that of capillaries. The prototype corrects defocus, astigmatism, and coma using a figure of merit based on the mean reflectance projection of a slab defined with real-time segmentation of retinal layers. AO correction with the ability to optimize focusing in arbitrary retinal depths – particularly the plexuses in the inner retina – could be achieved in 1.35 seconds. The AO-OCTA images showed greater flow signal, signal-to-noise ratio, and finer capillary caliber compared to commercial OCTA. Projection artifacts were also reduced in the intermediate and deep capillary plexuses. The instrument reported here improves OCTA image quality without excessive sacrifice in FOV and device complexity, and thus may have potential for clinical translation.

© 2020 Optical Society of America under the terms of the [OSA Open Access Publishing Agreement](#)

1. Introduction

Over the past decade, we have witnessed the rise of optical coherence tomographic angiography (OCTA) [1–4] in retinal imaging. Unlike fluorescein angiography, OCTA does not require intravenous dye injections and uses intrinsic motion contrast provided by the flowing blood cells. OCTA is acquired within a few seconds; making it ideal for translation into routine ophthalmic clinical practice. OCTA's three-dimensionality allows depth-resolved visualization of separate retinal plexuses [5] and the choriocapillaris, although projection artifacts pose a problem that needs to be dealt with in post-processing [6,7]. OCTA has been used to show capillary detail of the retinal vasculature or lack thereof [8], providing unprecedented details of neovascularization in diabetic retinopathy [9,10] and age-related macular degeneration (AMD) [1,11–16] as well as quantifiable differences in capillary perfusion or vascular topology of diseased and healthy eyes [17–21].

The rapid adoption of OCTA has been made possible by numerous hardware and software improvements. Novel algorithms that extract motion contrast from repeated B-scans have been successfully translated into commercial systems [22,23]. Two- and three-dimensional registration methods have improved the signal-to-noise ratio (SNR) of prototypes [24] and commercial systems [25,26] by averaging. On the hardware side, the speed has doubled every two years

allowing larger fields of view. Real time streaming and processing of images has become possible [27–29] allowing better quality acquisitions, and tracking devices have been incorporated [30]. Additionally, novel scanning protocols have been explored to reduce the prevalence of ocular motion artifacts [31–33], to increase the dynamic range [33], and to obtain velocimetric angiography [34].

One outstanding problem is the optical resolution of the instruments. The axial resolution in OCT depends on the central wavelength and bandwidth, whereas the lateral resolution depends on the numerical aperture (NA) of the imaging system, the aberrations introduced by ocular imperfections and the chromatic aberrations introduced by the source bandwidth. High lateral resolution is achieved by increasing the NA and using adaptive optics to compensate aberrations. Although adaptive optics OCTA (AO-OCTA) showing the true caliber of retinal capillaries has already been demonstrated [35–39], the achievable fields of view (FOV) were significantly limited. Insufficient FOV sets limitations on the clinical applicability of OCTA. There are fundamental tradeoffs between resolution and FOV. Higher NA and resolution is tied with smaller isoplanatic patches that limit the FOV in which the beam can be sharply focused. Smaller spot diameter also requires higher scanning density, which limits the achievable scan area within a tolerable scan time, which is generally 3–4 seconds without blinking. OCT systems described in the literature have so far clustered in the extreme ends of the tradeoff. Laboratory AO-OCT prototypes generally employed a high-NA, with the pupillary plane beam diameter of about 6 mm. These systems can produce outstanding resolution, but with limited FOV of less than 1 mm. On the other extreme, commercial OCT systems generally employ a low-NA, with the pupillary plane beam diameter of 1 to 1.2 mm. This allows a FOV of many mm but a focal spot size on the retinal plane of 15 to 20 μm , which is at least 2 times larger than capillary diameters. We believe the optimal trade-off for OCTA may lie in an intermediate NA that produces a focal spot diameter that is commensurate with capillary caliber of 4–7 μm [40,41].

In this manuscript, we have built an intermediate-NA AO-OCTA instrument that could image the parafoveal circulation within 3 seconds. The intermediate NA requires the correction of relatively fewer modes of higher-order aberrations, which is suitable for a sensorless design. Sensorless AO has several translational advantages over wavefront sensor-based instruments. The optical hardware complexity and cost is lower since the sensor, coupler, and many relay mirrors could be obviated. The footprint is further reduced because the optical design is based primarily on lenses rather than mirrors. However, sensorless AO comes with its own unique set of requirements. It relies on rapid estimation of the objective function to optimize focusing for specific tissue layers. We developed a fast and effective hill-climbing optimization algorithm with adaptive step size to compensate aberrations prior to OCTA acquisition with the prototype instrument [42]. Five low order Zernike modes were compensated within 1.35 seconds. This sensorless AO system incorporated real-time segmentation of the retinal layers, which allowed us to focus on the inner layers where retinal plexuses reside. This is yet another advantage over previous wavefront optimization mechanisms that tended to optimize focusing to the outer retinal layers where reflectance is strongest. Herein we demonstrate the benefits of this sensorless AO-OCTA instrument in producing OCTA images with improved contrast, SNR, and visualization of capillary caliber, as well as reduced prevalence of projection artifacts, all of that with a moderate sacrifice in FOV.

2. Materials and methods

2.1. Data acquisition

Subjects were scanned over 0.75×.75 mm, 1.5×1.5 mm, 2×2 mm, and 3.3×3.3 mm FOVs in a single shot with a 250-kHz AO-OCTA prototype built at the Center for Ophthalmic Optics and Lasers (COOL Lab) of the Casey Eye Institute (Fig. 1). All FOVs were acquired with scan density of 600 A-lines × 1200 B-scans, which includes two repetitions at each B-scan position.

Scans sized 2×2 mm centered on the fovea were also acquired with a 70-kHz commercial, spectral-domain OCT system (Avanti, Optovue, Inc., Fremont, CA), consisting of 304 A-lines \times 608 B-scans. Instead of placing the pupil-conjugated deformable mirror on axis and using the classic combination of a pair of wave plate and polarization beam splitter [43], we placed it at an incidence angle of 8 degrees (Fig. 1) to reduce the optical losses of the sample arm. Besides the telescope placed to steer the beam through the pupil, another telescope was used to reduce the beam diameter from the aperture of the deformable mirror (10.5 mm) to the aperture of the galvo scanners (5 mm). The entire sample arm fitted in a $12'' \times 12''$ breadboard (Fig. 1).

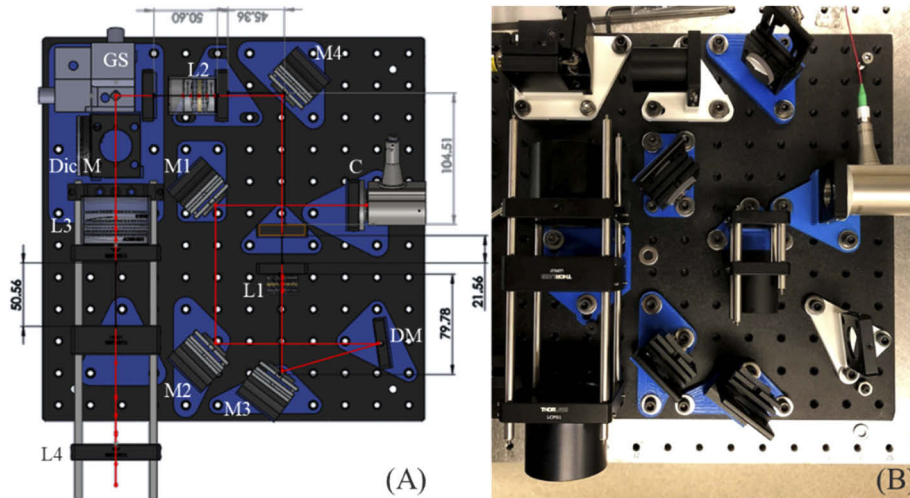


Fig. 1. Setup of the sample arm of AO-OCTA system. (A) shows the CAD design done in SolidWorks and (B) a picture of the sample arm on a $12'' \times 12''$ breadboard. A fiber coupler (90%-10%, Gould Fiber Optics) directs the light from the superluminescent diode (M-D-840-HP, Superlum) through a reflective collimator into the sample arm shown in (A). C – Reflective collimator (Thorlabs, Inc.) M1-M4 – Mirrors. L1-L4 – Lenses with focal length of 150 mm, 60 mm, 100 mm and 75 mm respectively. GS – Galvo scanner (Cambridge Technologies). DM – Deformable mirror (DM69, ALPAO, Inc.). Dic M – Dichroic mirror redirecting visible light to an upper level with the fixation target. A spectrometer (Cobra-S 800, Wasatch photonics) with a 2048-pixel camera (Octoplus, Teledyne e2v) was used to read the OCT interferograms. Optical fiber patches were added to the sample and reference arms to compensate delay and dispersion. A dummy mirror was placed at the position of the deformable mirror in the picture for alignment purposes. Spacers were 3D printed. The sample arm efficiency was 75%.

Both systems had light sources centered at 840-nm wavelength. The commercial system had a 50-nm bandwidth, yielding an axial resolution of $5 \mu\text{m}$ in tissue whereas the prototype's source had an effective 91-nm bandwidth, for an axial resolution of approximately $3 \mu\text{m}$. The axial digital sampling was $3 \mu\text{m}$ for the commercial system and $2 \mu\text{m}$ for the prototype by using a Cobra-S 800 spectrometer (Wasatch photonics, Inc.) with a 2048-pixel camera (Octoplus, Teledyne e2v). In terms of lateral resolution, the prototype could correct five low-order aberrations by controlling a deformable mirror (DM 69, ALPAO Inc., France) containing 69 actuators that allowed a theoretical optical resolution of $6 \mu\text{m}$ (Fig. 2), whereas the commercial system's resolution was $15 \mu\text{m}$. The system was designed with an intermediate NA of ~ 0.1 (beam diameter = 3.2 mm on pupil) to reduce the visualized caliber of capillaries with respect to commercial OCTA and increase the FOV with respect to high-NA AO-OCT instruments; allowing single run, non-mydratic scanning of a clinically useful FOV. The transverse sampling densities for the

2×2 mm scanning protocol were 6.5 $\mu\text{m}/\text{pixel}$ for the commercial system and 3.3 $\mu\text{m}/\text{pixel}$ for the AO-OCTA prototype. The tracking system available in the commercial system was activated to reduce the prevalence of motion artifacts [30].

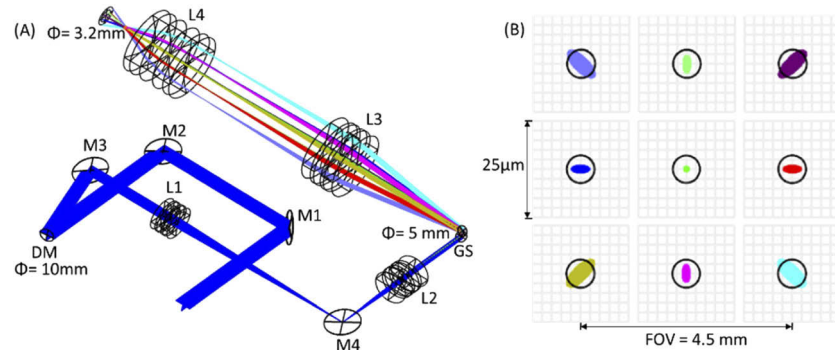


Fig. 2. Simulation of the system's optical performance in OpticStudio (Zemax). (A) Ray trace simulation. (B) Simulation of the beam size ($\approx 6 \mu\text{m}$) over a field of view of 4.5 mm centered at the fovea of an emmetropic eye model.

Participants were recruited from the Casey Eye Institute at the Oregon Health & Science University (OHSU). The protocol was approved by the Institutional Review Board/Ethics Committee of OHSU and the research adhered to the tenants of the Declaration of Helsinki.

2.2. Data processing

Flow signal in both the prototype and the commercial system was generated by the split-spectrum amplitude-decorrelation (SSADA) algorithm [1,22], computed from the two overlapping B-scans acquired at each position. In SSADA, the speckle variances of OCT B-scans generated for different spectral bands of interferometric signal yielding the OCT B-scan images are averaged, improving the signal-to-noise ratio of flow detection over full-bandwidth speckle decorrelation measurement. Previous work using the commercial Avanti system has shown the number of spectral Gaussian splits for optimal SSADA implementation was 11 [44]. Because our AO-OCT prototype has a wider spectrum, it allowed a larger number of splits. In our case, twenty-three splits yielded the highest SNR (Fig. 3), each having a bandwidth of 18 nm with their centers separated by 3.5 nm from the neighboring Gaussian windows.

Because AO-OCTA has a reduced depth of focus with respect to commercial OCTA, the focusing of acquisitions was optimized for the inner retinal layers (between the inner limiting membrane and the outer plexiform layer) where the retinal plexuses reside [45]. Retinal layers were segmented using a U-Net type fully-convolutional neural network for *en face* projection presentation of the layers and plexuses of interest. Annotations for generating training datasets were obtained with a recent graph-cut algorithm [46] and manual corrections. To make U-Net inferencing available in real-time, TensorRT was used to prune and fuse some of the layers in our implementation of U-Net, and reduced float32 precision to int8, while preserving the network performance. Tensor Cores in GPU were also used to increase substantially the speed of convolutional operations. Network training and inference was performed on B-scans after averaging 10 consecutive frames and performing rigid registrations to compensate moderate displacements between them caused by involuntary ocular motion [47].

En face images of the superficial vascular complex (SVC), intermediate capillary plexus (ICP) and deep capillary plexus (DCP) were generated by maximum projection of OCTA decorrelation values. In order to remove microsaccadic artifacts, two redundant OCTA scans of the same FOV were acquired and registered. For the AngioVue system, a proprietary registration algorithm

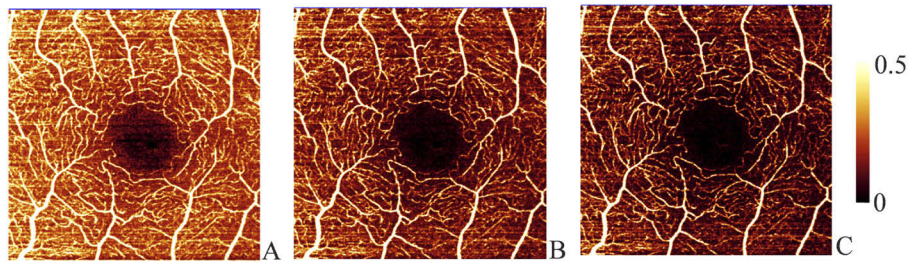


Fig. 3. Increasing the number of spectral splits with respect to previous SSADA implementations [1,22] allowed increasing the flow signal-to-noise ratio (SNR) while maintaining the sharpness of capillaries in *en face* angiogram visualizations. The superficial vascular complex is demonstrated. Flow SNR increases from 5.6 for the 11 spectral splits (A, bandwidth of 27 nm, separated by 6.6 nm) to 9.5 for 18 spectral splits (B, bandwidth of 20 nm, separated by 4.3 nm) and 11.2 for 23 spectral splits (C, bandwidth of 18 nm, separated by 3.5 nm). Greater number of spectral splits did not yield further SNR improvement on *en face* OCTA projections.

merged two consecutive raster scans acquired in orthogonal scanning priorities [48]. For the AO-OCTA prototype, these artifacts were removed by parallel strip registration (Fig. 4) [49,50].

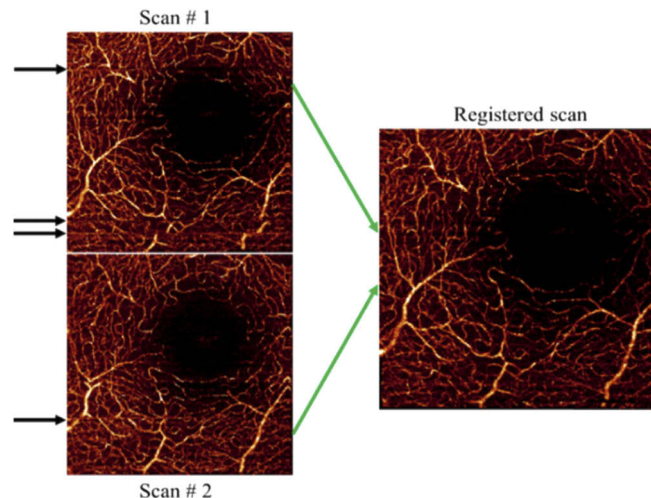


Fig. 4. Removal of motion artifacts by parallel-strip registration of two redundant scans of the same FOV acquired with the AO-OCTA prototype. Black arrows indicate the position of motion artifacts in the original scans.

Real time rendering of OCT [28] and OCTA [29] volumes on GPU was incorporated into our acquisition software OCTViewer, allowing video-rate streaming of OCT and OCTA cross-sectional and *en face* visualizations of AO prototype acquisitions. The desktop computer controlling the acquisition components contained an Intel Core i9 9900k CPU and a NVIDIA Titan RTX GPU, running on Windows 10 with CUDA release v10.2. Rather than saving the data captured after the operator clicks on acquisition, the AO-OCTA prototype operates in continuous acquisition mode and allowed the operator to wait for a high-quality scan and save the data currently present in the buffer. By continuously rendering the OCT and OCTA *en face* projections of the layer of interest as well as real-time streaming of B-scans, we helped the operator reduce

the prevalence of blinks, motion and vignetting artifacts by improving the judgement of scan quality prior to acquisition.

2.3. Sensorless optimization of human eye aberrations by AO-OCTA prototype

The figure of merit used to guide the optimization of ocular aberrations was the average value of the mean reflectance projection within the slab of interest. It was calculated from undersampled OCT data acquired at a rate of 33 volumes/s. Nine figures of merit were acquired per Zernike mode, which estimated the critical point of objective functions for defocus, vertical and oblique astigmatism, and vertical and horizontal coma in a sequential fashion [42]. Sensorless sampling of the unknown objective function was determined by a hill climbing optimization with adaptive step size, which uses the cumulative sign of the gradient to determine the step and is assisted by a quadratic fitting of three figure of merit values estimated to reside at the vicinity of the objective function critical point [42]. Optimization took only 1.35 seconds (Fig. 5), and the hill-climbing method minimized the detrimental effects of hysteresis and avoided searching near the end of the deformable mirror's dynamic range, where figures of merit cannot be produced reliably due to low signal quality. After optimization, subjects were allowed to blink before the subsequent OCTA acquisition took place. We have previously demonstrated that this sensorless optimization routine was highly reproducible between blinks and robust to involuntary ocular motion [42].

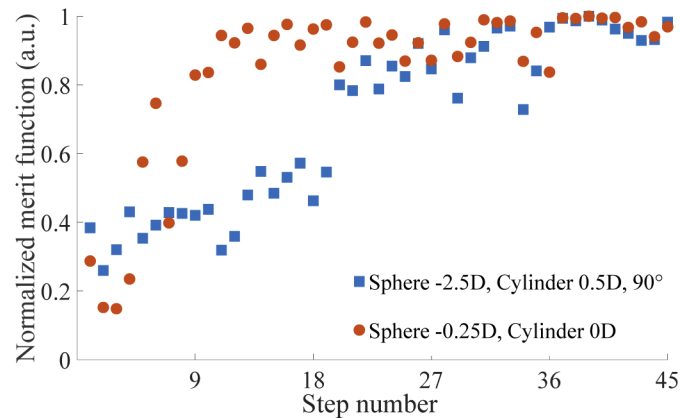


Fig. 5. Comparison of the figure of merit evolution normalized to its maximum value, during the optimization of ocular aberrations prior to OCTA acquisition for an astigmatic and a non-astigmatic subject. Each point represents the mean value of the reflectance OCT projection of the slab/layer of interest from a volume acquired in high-speed mode at a rate of 33 volumes per second. The non-astigmatic subject reached its optimal correction after the first mode (defocus, first nine steps) whereas the astigmatic subject reached its optimal correction after oblique and vertical astigmatism had been optimized (first 27 steps). The entire process (45 figures of merit computed, 9 per mode) was completed within 1.35 seconds.

2.4. Quantitative comparison with commercial OCTA

Images acquired by the commercial and AO prototype instruments were compared by flow SNR, prevalence of projection artifacts, capillary caliber, and vessel density. The flow SNR was found from the signal of the foreground (vascular pixels) and the signal of the 0.3-mm radius foveal avascular zone (FAZ),

$$SNR = \frac{\bar{D} - \overline{D_{FAZ}}}{\sqrt{\sigma_{D_{FAZ}}^2}} \quad (1)$$

where \bar{D} represents the mean decorrelation value and $\sigma_{D_{FAZ}}$ represents the standard deviation of the background decorrelation. The vessel density values were calculated from the binary vascular masks generated using our previous thresholding scheme based on the regression analysis of the relationship between decorrelation and reflectance of the background voxels [51]. It was calculated as the percentage of vascular pixels, excluding the central 0.6-mm diameter circular area co-centered with the FAZ.

The prevalence of projection artifacts was also compared between the two instruments. It has been demonstrated previously that AO-OCTA reduces the effect of this common artifact [36], which confounds the visualization and quantification of capillary perfusion in the ICP and DCP. This benefit of AO was attributed to the tighter depth of focus of the optical beam projected on the retina. In the current work using a looser depth of focus than [36], we investigate the prevalence of this artifact by computing the cross-correlation coefficient of the ICP and DCP with the SVC in both AO and commercial OCTA instruments. We then compared vessel density with respect to the AO-OCTA images.

The capillary caliber yielded by both instruments was calculated by finding the ratio between the number of vascular pixels in the vascular binary masks and the number of pixels in a skeletonized binary mask.

A paired t-test was used to evaluate the statistical significance of all AO prototype and commercial OCTA comparisons.

3. Results

The retinal blood flow of eleven healthy eyes from eleven subjects (35 ± 2 years old) with -1 to 3 diopters of defocus and -1 to 0.5 diopters of astigmatism was imaged with OCTA on both instruments over a 2×2 mm FOV centered at the fovea and focusing on the inner retina. These eyes were also imaged at different eccentricities (up to 5-degrees superior and nasal to the fovea) and fields of view (3×3 mm, 1.5×1.5 mm and 0.75×0.75 mm) with the AO-OCTA prototype only.

Because the depth-of-focus of the AO-OCTA prototype ($58 \mu\text{m}$) is shorter than the retinal width, layer-specific focusing was essential to maintaining good quality OCTA (Fig. 6). If the figure of merit used for optimization of defocus was dominated by outer-retinal reflectance values (Fig. 6(B)), OCTA of the inner retinal flow would yield low quality *en face* angiograms (Fig. 6(D)).

Prevalence of projection artifacts measured as cross-correlation with SVC was reduced significantly by the AO-OCTA prototype with respect to the commercial instrument (blue arrows in Fig. 7) in both the ICP (AO-OCT 0.45 ± 0.07 vs Commercial 0.69 ± 0.02 , $p < 0.01$) and the DCP (AO-OCT 0.07 ± 0.04 vs Commercial 0.35 ± 0.07 , $p < 0.01$). The AO-OCTA instrument yielded higher contrast than commercial OCTA on this plexuses ($p < 0.01$), visualized in higher detail in the areas surrounded by dashed lines in Fig. 7.

The high capillary contrast and low correlation of the ICP and DCP with the SVC capillary networks was observed for all eccentricities and fields of view explored (Fig. 8), including the most clinical useful landmarks, i.e. the parafoveal and peripapillary regions.

The vessel density measured by the AO-OCTA prototype was reduced for all plexuses ($p < 0.01$, Table 1). Because the flow SNR was also considerably higher for AO-OCTA (Table 1), the reduction in vessel density could not be due to reduced OCTA signal. The combination of a thinner apparent capillary caliber and reduced prevalence of projection artifacts using adaptive optics worked together to reduce the measured vessel density. Indeed, the capillary diameters obtained by AO-OCTA (Table 2) lied between $7 \mu\text{m}$ and $9 \mu\text{m}$ - which are values closer to the real caliber, whereas the capillary diameter measured on OCTA produced by the commercial instrument was between 12 - $14 \mu\text{m}$.

Parallel-strip registration could also be applied for more than two scans (Fig. 9). The real-time rendering feature of the acquisition software allowed the operator to wait for the right acquisition

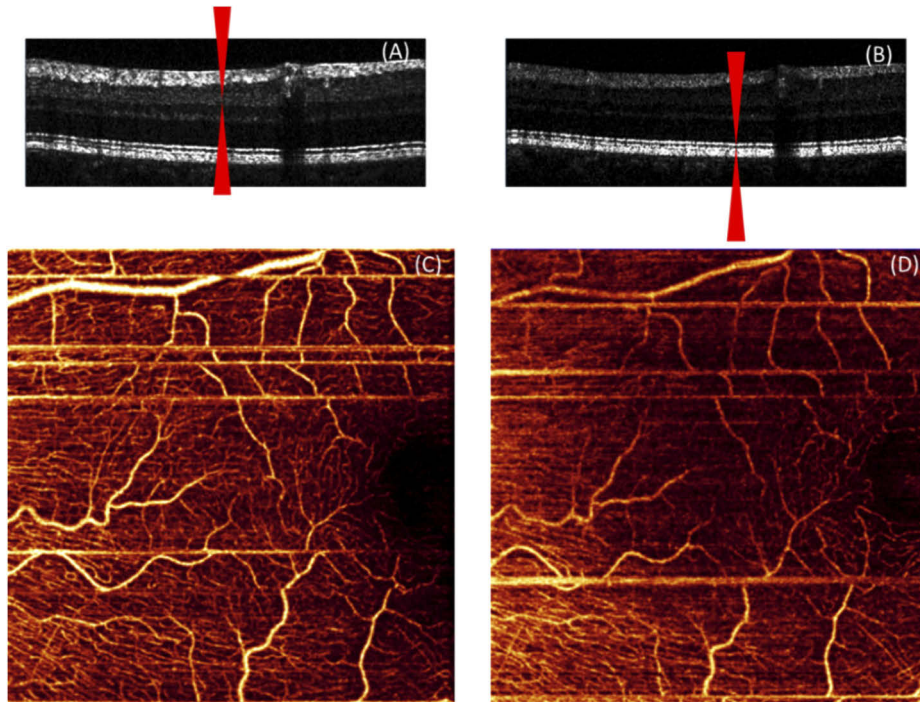


Fig. 6. Layer-specific optimization of focusing using sensor-less AO with real-time image processing segmentation of retinal layers. (A) Focusing with a figure of merit based on the inner retina layers produces a cross-sectional OCT image with bright inner layers. (B) A figure of merit based on the entire B-frame bring the focus to the outer retina with its highly backscattering ellipsoid zone – retinal pigment epithelium complex. (C) Focusing on the inner retina optimizes the sharpness of retinal OCTA. (D) Focusing on the outer retina blurs the retinal OCTA. Field of view is 3.3×3.3 mm.

Table 1. Comparison of signal-to-noise ratio and vessel density between AO-OCTA and commercial OCTA.^a

	Flow SNR*	Vessel density (%)*		
		SVC	ICP	DCP
AO-OCTA	8.6 ± 3.3	23.3 ± 1.9	25.8 ± 1.7	25.0 ± 3.0
Commercial OCTA	1.0 ± 1.0	44.0 ± 7.4	36.0 ± 4.5	30.3 ± 2.9

^aScans of 11 healthy eyes over a 2×2 mm FOV centered at fovea

Table 2. Comparison of capillary caliber observed in the retinal plexuses with AO-OCTA and commercial OCTA.^a

	Capillary caliber (μm)*		
	SVC	ICP	DCP
AO-OCTA	7.8 ± 0.6	8.4 ± 0.5	8.6 ± 0.5
Commercial OCTA	14.3 ± 0.7	12.9 ± 0.5	12.3 ± 0.3

^aScans of 11 healthy eyes over a 2×2 mm FOV centered at fovea

instant where the minimal amount of blinks and microsaccadic artifacts were present and acquire the data being rendered in real time. This reduced the probability of overlapping microsaccades, which challenges the success of parallel-strip registration.

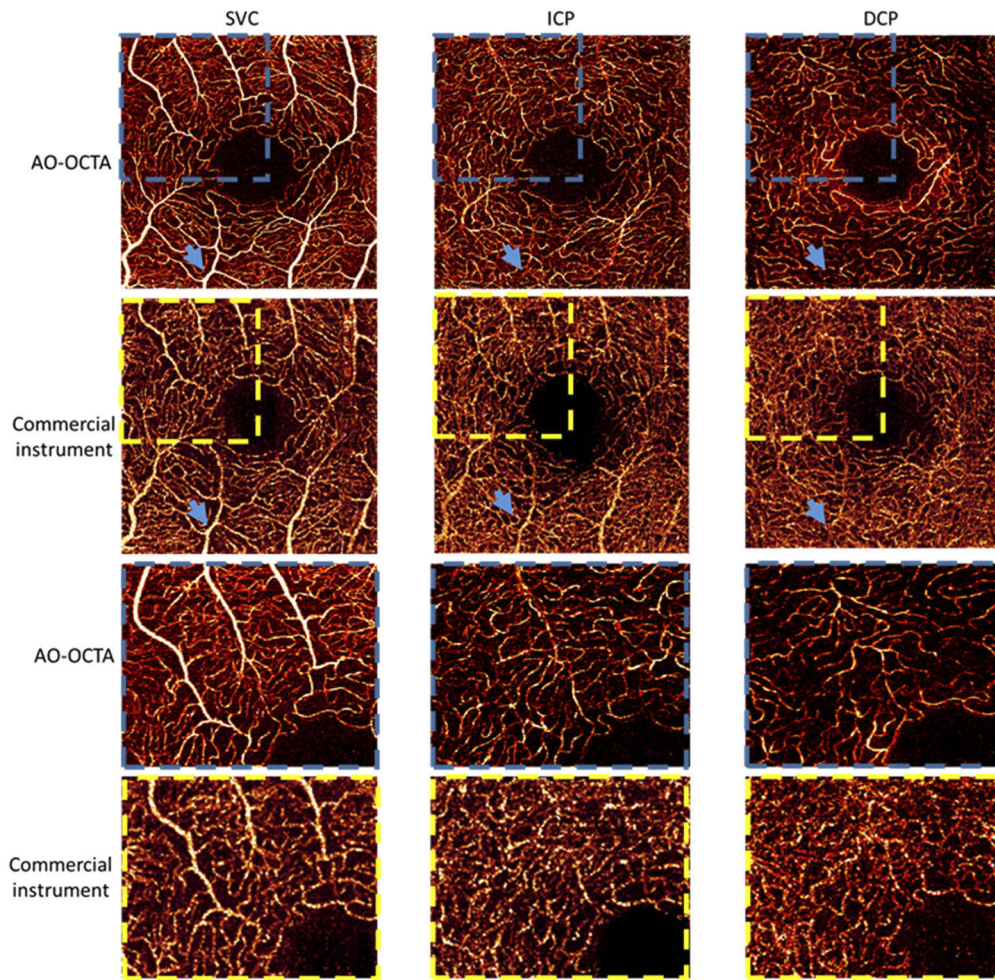


Fig. 7. Superficial vascular complex (SVC), intermediate capillary plexus (ICP) and deep capillary plexus (DCP) show better contrast in the images acquired by the AO-OCTA prototype compared to the images acquired by the commercial instrument. Upper-left corners were enlarged to better visualize the difference in contrast. Projection artifacts were visibly reduced (e.g. the locations marked by blue arrows) by AO-OCTA without using any projection removal post-processing algorithm. FOV is 2×2 mm for both instruments.

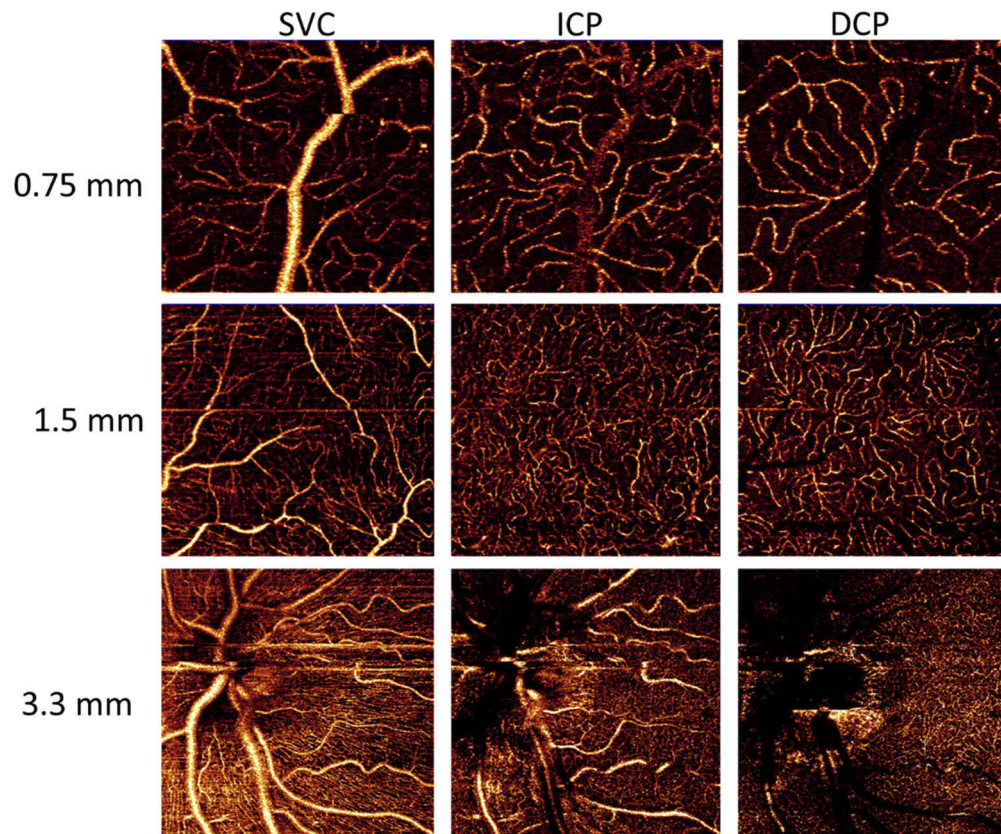


Fig. 8. OCTA of FOV of 0.75×0.75 mm at 5 degrees superior to the fovea, 1.5×1.5 mm at 5 degrees nasal to the fovea and 3.3×3.3 mm of the peripapillary area, acquired from an eye with -0.5 diopters of defocus and 0.25 diopters of astigmatism. High capillary contrast is observed for the superficial vascular complex (SVC), intermediate capillary plexus (ICP) and deep capillary plexus (DCP). The low prevalence of OCTA projection artifacts is visualized on ICP and DCP images.

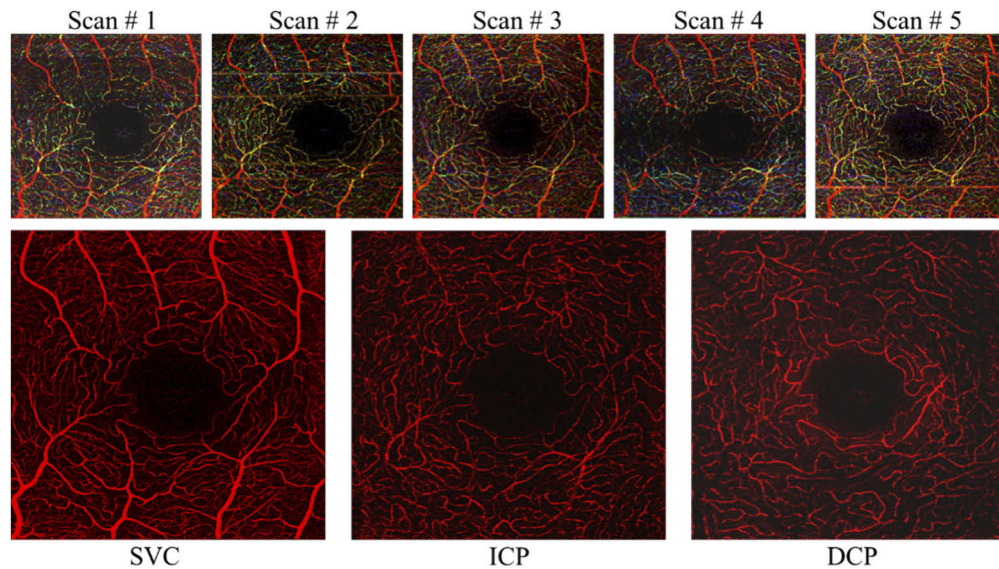


Fig. 9. Parallel-strip registration of retinal angiograms of the superficial vascular complex (SVC), intermediate capillary plexus (ICP) and deep capillary plexus (DCP) acquired with the AO-OCTA prototype resulting in high contrast and removal of projection and vignetting artifacts observed with random prevalence in single scans. The top row shows inner retinal flow is represented in single scans in an RGB color scheme (red – SVC flow, green – ICP, blue – DCP).

4. Discussion and conclusions

In this work, we have demonstrated a high-speed, spectral-domain sensorless AO-OCTA instrument to image retinal capillaries of all retinal plexuses simultaneously with high resolution. Improved visualization of the intermediate and deep plexuses with respect to commercial OCTA was demonstrated. With the addition of post-processing motion correction by parallel-strip registration, AO-OCTA provided depth-resolved and motion-artifact-free angiograms of the retinal blood flow with outstanding capillary resolution. Although this prototype has only been demonstrated for healthy eyes, the optimization of aberrations should also be successful in future imaging of diseases of interest such as diabetic retinopathy and AMD.

AO-OCTA improves the caliber of capillaries by refining the optical resolution of the scanning beam. Therefore, when the beam samples vascular pixels, the OCTA decorrelation is less likely diluted by the influence of adjacent static signal encompassed in the point spread function. Consequently, we observed a larger SNR for AO-OCTA images although (1) the inter B-scan time was half that of the commercial instrument and (2) higher resolution can also increase the background signal in the event of bulk motion during scanning or beam repositioning errors.

High-NA instruments designed for visualization of cone and rod photoreceptors can exhibit outstanding capillary resolution but reduce considerably the effective FOV and available depth of focus. Our intermediate-NA system scans the retina with a beam spot of 6 μm , a diameter within the range of capillary thickness that allows larger FOV and depth of focus. The area covered by the FOVs demonstrated here is sufficient to extract foveal biomarkers and parafoveal perfusion density from OCTA, biomarkers with great potential in clinical evaluation. The 58 μm depth of focus was sufficient to image the three plexuses but it was still less than the whole retinal thickness. Thus, separate focusing would be needed to obtain high quality OCTA of outer retinal (e.g. choroidal neovascularization, CNV) and choroidal flow (e.g. choriocapillaris). This is a

disadvantage in comparison to low-NA commercial OCTA systems, which could image both retinal and choroidal circulations simultaneously.

The capability to optimize defocus for any arbitrary layer has been a challenge for both sensed and sensorless AO instruments. With the advent of high-speed OCTA systems and the use of GPU computation, it is now possible to optimize the inner retinal flow by minimizing aberrations using a three-dimensional figure of merit extracted from volumes acquired at a rate of several Hz and with real-time tracking of the retinal depth desired. Here, the sensorless optimization routine prior to OCTA acquisition took only 1.35 seconds to correct inner-retinal specific defocus together with oblique and vertical astigmatism, as well as horizontal and vertical coma. In contrast, commercial instruments not using adaptive optics only correct for defocus and need to reduce the NA in order to assume the remaining aberrations negligible.

Despite OCTA's advantages over fluorescein angiography, a historical limitation of OCTA has been the smaller FOV. Because of the constraint imposed by the shorter depth of focus, adaptive optics instruments restrain OCTA's FOV even further. Designs like ours based on intermediate-NA imaging beams [52] alleviate this problem and present a potential to either achieve a clinically useful FOV in a single scan or to reduce the number of acquisitions needed for larger FOVs by montaging partially overlapping scans. We have recently estimated that for an intermediate NA instrument we can compensate aberrations homogeneously over a FOV up to 2.5 mm [42]. Although that FOV for a single scan is about 4 times larger than typical AO, it is still smaller than the FOV currently achievable with commercial OCTA. Some clinical applications such as imaging the CNV in AMD might still require stitching with scans acquired at adjacent positions.

A limitation of the instrument presented here is the scanning speed. Although 250 kHz is for a spectral domain system higher than any speed commercially available, the smaller beam spot using AO demands a proportionally more sampling points, effectively increasing the volume acquisition time and consequently the prevalence of blinks and microsaccadic artifacts. With the scanning density used here ($600 \times 600 \times 2$) an isotropic scanning pattern was completed with sufficient sampling and within approximately 3 seconds, which is a reasonable fixation time when tracking hardware is not used.

One benefit of AO-OCTA is the reduction of projection artifacts. This artifact manifests as a projection of the superficial vascular network flow signal on top of the underlying capillary plexuses, outer retina and choriocapillaris; hindering the visualization of in situ flow. Projections are reduced in AO-OCTA because with the tighter focusing achieved by the higher NA, the incident beam is less likely to be significantly perturbed by the moving blood cells in the superficial vessels during forward propagation [36]. Projection-resolved OCTA (PR-OCTA) algorithms have been successfully implemented previously on commercial OCTA [6,7]. These algorithms might occasionally remove true flow pixels affecting the vessel continuity, or be unable to remove the whole projection signal. With an already lower projection prevalence in AO-OCTA, we expect that PR algorithms applied synergistically with AO-OCTA can yield an even better projection removal. Accurately removing this artifact holds a significant clinical application in better measuring the perfusion density of the ICP and DCP for diabetic retinopathy, retinal vein occlusion and other vascular diseases. It would also improve the specificity and therefore accuracy of CNV detection in advanced AMD. In tandem with AO focusing correction for arbitrary depths, it could also improve the accuracy of capillary density measurement in the choriocapillaris and lamina cribrosa, which are active areas of research. However, a disadvantage of AO-OCTA is that large superficial vessels cast shadows instead of projections, and in situ flow signal becomes irretrievable (e.g. DCP in Figs. 7 & 8). This is caused by the "shower curtain" effect, in which the influence of scattering on OCT signal attenuation increases with distance from the scatterer. See how ICP in Figs. 7 and 8 does not show the shadows observed in DCP. Although these shadows are more prominent in AO-OCTA, they do not account for as many

pixels as projection artifacts do in commercial OCTA, and can be excluded with high accuracy by post-processing [53].

The improved resolution with AO-OCTA is potentially useful for visualizing vascular malformations such as intraretinal microvascular abnormalities (IRMAs), microaneurysms, and dilated capillaries, which are barely recognizable with current commercial OCTA. The presence of IRMAs is one of the features used by the Early Treatment Diabetic Retinopathy Study (ETDRS) to determine severe non-proliferative diabetic retinopathy (NPDR) [54]. Diagnosing the severe stage is significant because the risk of progression to proliferative DR within a year is 50% [55]. In neovascular AMD, AO could improve the visualization of CNV with OCTA. CNV often presents in patterns of coralliform complexes or thin capillaries growing from a feeding trunk. It has been hypothesized that proliferation of thin capillary networks (and not large stable arterialized trunks) on OCTA corresponds to the reactivation of vascular endothelial growth factor (VEGF activity) for CNV under anti-VEGF treatment [56]. In principle, AO could help better characterize CNV morphology. Additionally, AO-OCTA could improve the ability to detect mildly reduced flow states where the capillary caliber may be reduced without complete cessation for flow and disappearance of the capillary on OCTA. Finally, AO-OCTA could also assist in imaging polypoidal flow in polypoidal choroidal vasculopathy (PCV). OCT images of PCV are characterized by dome-shaped pigment epithelial detachments (PED) and hyper-reflective spots near the level of the Bruch's membrane, indicative of polypoidal activity [53]. The potential for AO in PCV lies in the promise to improve the discrimination of the decorrelation signal in polyp voxels from background when imaged with OCTA.

Funding

Research to Prevent Blindness (Mary Greve Special Scholar Award, Unrestricted departmental funding grant); National Eye Institute (P30 EY010572, R01 EY023285, R01 EY024544, R01 EY027833).

Disclosures

Acner Camino: Optovue, Inc (P). Yali Jia: Optovue, Inc (F, P). David Huang: Optovue, Inc (F, I, P, R), Yifan Jian: Seymour Vision (I). These potential conflicts of interest have been reviewed and managed by OHSU. Other authors declare that there are no conflicts of interest related to this article.

References

1. Y. Jia, S. T. Bailey, T. S. Hwang, S. M. McClintic, S. S. Gao, M. E. Pennesi, C. J. Flaxel, A. K. Lauer, D. J. Wilson, J. Hornegger, J. G. Fujimoto, and D. Huang, "Quantitative optical coherence tomography angiography of vascular abnormalities in the living human eye," *Proc. Natl. Acad. Sci.* **112**(18), E2395–E2402 (2015).
2. S. S. Gao, Y. Jia, M. Zhang, J. P. Su, G. Liu, T. S. Hwang, S. T. Bailey, and D. Huang, "Optical Coherence Tomography Angiography," *Invest. Ophthalmol. Visual Sci.* **57**(9), OCT27–OCT36 (2016).
3. C.-L. Chen and R. K. Wang, "Optical coherence tomography based angiography [Invited]," *Biomed. Opt. Express* **8**(2), 1056–1082 (2017).
4. R. F. Spaide, J. G. Fujimoto, N. K. Waheed, S. R. Sadda, and G. Staurengi, "Optical coherence tomography angiography," *Prog. Retinal Eye Res.* **64**, 1–55 (2018).
5. T. S. Hwang, M. Zhang, K. Bhavsar, X. Zhang, J. P. Campbell, P. Lin, S. T. Bailey, C. J. Flaxel, A. K. Lauer, D. J. Wilson, D. Huang, and Y. Jia, "Visualization of 3 distinct retinal plexuses by projection-resolved optical coherence tomography angiography in diabetic retinopathy visualization of retinal plexuses in diabetic retinopathy visualization of retinal plexuses in diabetic retinopathy," *JAMA Ophthalmol.* **134**(12), 1411–1419 (2016).
6. J. Wang, M. Zhang, T. S. Hwang, S. T. Bailey, D. Huang, D. J. Wilson, and Y. Jia, "Reflectance-based projection-resolved optical coherence tomography angiography [Invited]," *Biomed. Opt. Express* **8**(3), 1536–1548 (2017).
7. M. Zhang, T. S. Hwang, J. P. Campbell, S. T. Bailey, D. J. Wilson, D. Huang, and Y. Jia, "Projection-resolved optical coherence tomographic angiography," *Biomed. Opt. Express* **7**(3), 816–828 (2016).
8. Y. Guo, A. Camino, J. Wang, D. Huang, T. S. Hwang, and Y. Jia, "MEDnet, a neural network for automated detection of avascular area in OCT angiography," *Biomed. Opt. Express* **9**(11), 5147–5158 (2018).

9. T. S. Hwang, Y. Jia, S. S. Gao, S. T. Bailey, A. K. Lauer, C. J. Flaxel, D. J. Wilson, and D. Huang, "Optical coherence tomography angiography features of diabetic retinopathy," *Retina* **35**(11), 2371–2376 (2015).
10. Q. You, Y. Guo, J. Wang, X. Wei, A. Camino, P. Zang, C. J. Flaxel, S. T. Bailey, D. Huang, Y. Jia, and T. S. Hwang, "Detection of clinically missed retinal neovascularization with wide-field optical coherence tomography angiography," *Retina* (2019).
11. A. D. Treister, P. L. Nesper, A. E. Fayed, M. K. Gill, R. G. Mirza, and A. A. Fawzi, "Prevalence of Subclinical CNV and Choriocapillaris Nonperfusion in Fellow Eyes of Unilateral Exudative AMD on OCT Angiography/Treister et al.," *Trans. Vis. Sci. Tech.* **7**(5), 19 (2018).
12. M. Arya, C. B. Rebhun, E. D. Cole, A. S. Sabrosa, G. Arcos-Villegas, R. N. Louzada, E. A. Novais, M. Lane, S. Dang, M. Ávila, A. J. Witkin, C. R. Bauman, J. S. Duker, and N. K. Waheed, "Visualization of choroidal neovascularization using two commercially available spectral domain optical coherence tomography angiography devices," *Retina* **39**(9), 1682–1692 (2019).
13. J. R. de Oliveira Dias, Q. Zhang, J. M. B. Garcia, F. Zheng, E. H. Motulsky, L. Roisman, A. Miller, C.-L. Chen, S. Kubach, L. de Sistiernes, M. K. Durbin, W. Feuer, R. K. Wang, G. Gregori, and P. J. Rosenfeld, "Natural History of Subclinical Neovascularization in Nonexudative Age-Related Macular Degeneration Using Swept-Source OCT Angiography," *Ophthalmology* **125**(2), 255–266 (2018).
14. L. Roisman, Q. Zhang, R. K. Wang, G. Gregori, A. Zhang, C.-L. Chen, M. K. Durbin, L. An, P. F. Stetson, G. Robbins, A. Miller, F. Zheng, and P. J. Rosenfeld, "Optical coherence tomography angiography of asymptomatic neovascularization in intermediate age-related macular degeneration," *Ophthalmology* **123**(6), 1309–1319 (2016).
15. R. Told, S. Sacu, A. Hecht, M. Baratsits, K. Eibenberger, M. E. Kroh, S. Rezar-Dreindl, F. G. Schlanitz, G. Weigert, A. Pollreis, and U. Schmidt-Erfurth, "Comparison of SD-optical coherence tomography angiography and indocyanine green angiography in type 1 and 2 neovascular age-related macular degeneration OCTA ICGA comparison in nAMD," *Invest. Ophthalmol. Visual Sci.* **59**(6), 2393–2400 (2018).
16. M. Al-Sheikh, N. A. Iafe, N. Phasukkijwatana, S. R. Sadda, and D. Sarraf, "Biomarkers of neovascular activity in age-related macular degeneration using optical coherence tomography angiography," *Retina* **38**(2), 220–230 (2018).
17. P. L. Nesper, P. K. Roberts, A. C. Onishi, H. Chai, L. Liu, L. M. Jampol, and A. A. Fawzi, "Quantifying microvascular abnormalities with increasing severity of diabetic retinopathy using optical coherence tomography angiography parameters correlate with DR Severity," *Invest. Ophthalmol. Visual Sci.* **58**(6), BIO307 (2017).
18. J. Schottenhamml, E. M. Moul, S. Ploner, B. Lee, E. A. Novais, E. Cole, S. Dang, C. D. Lu, L. Husvagt, N. K. Waheed, J. S. Duker, J. Horneegger, and J. G. Fujimoto, "An automatic, intercapillary area-based algorithm for quantifying diabetes-related capillary dropout using optical coherence tomography angiography," *Retina* **36**(Suppl 1), S93–S101 (2016).
19. B. D. Krawitz, E. Phillips, R. D. Bavier, S. Mo, J. Carroll, R. B. Rosen, and T. Y. P. Chui, "Parafoveal nonperfusion analysis in diabetic retinopathy using optical coherence tomography angiography," *Trans. Vis. Sci. Tech.* **7**(4), 4 (2018).
20. L. Liu, B. Alonzo, H. Takusagawa, J. C. Morrison, B. Edmunds, S. Tehrani, Y. Jia, and D. Huang, "Optical coherence tomography angiography of peripapillary retina pre- and post-trabeculectomy," *Invest. Ophthalmol. Visual Sci.* **59**, 5057 (2018).
21. B. D. Krawitz, S. Mo, L. S. Geyman, S. A. Agemy, N. K. Sripsema, P. M. Garcia, T. Y. P. Chui, and R. B. Rosen, "Acircularity index and axis ratio of the foveal avascular zone in diabetic eyes and healthy controls measured by optical coherence tomography angiography," *Vision Res.* **139**, 177–186 (2017).
22. Y. Jia, O. Tan, J. Tokayer, B. Potsaid, Y. Wang, J. J. Liu, M. F. Kraus, H. Subhash, J. G. Fujimoto, J. Horneegger, and D. Huang, "Split-spectrum amplitude-decorrelation angiography with optical coherence tomography," *Opt. Express* **20**(4), 4710–4725 (2012).
23. R. K. Wang, L. An, P. Francis, and D. J. Wilson, "Depth-resolved imaging of capillary networks in retina and choroid using ultrahigh sensitive optical microangiography," *Opt. Lett.* **35**(9), 1467–1469 (2010).
24. P. Zang, G. Liu, M. Zhang, J. Wang, T. S. Hwang, D. J. Wilson, D. Huang, D. Li, and Y. Jia, "Automated three-dimensional registration and volume rebuilding for wide-field angiographic and structural optical coherence tomography," *J. Biomed. Opt.* **22**(2), 026001 (2017).
25. A. Camino, M. Zhang, C. Dongye, A. D. Pechauer, T. S. Hwang, S. T. Bailey, B. Lujan, D. J. Wilson, D. Huang, and Y. Jia, "Automated registration and enhanced processing of clinical optical coherence tomography angiography," *Quant. Imaging Med. Surg.* **6**(4), 391–401 (2016).
26. M. F. Kraus, B. Potsaid, M. A. Mayer, R. Bock, B. Baumann, J. J. Liu, J. Horneegger, and J. G. Fujimoto, "Motion correction in optical coherence tomography volumes on a per A-scan basis using orthogonal scan patterns," *Biomed. Opt. Express* **3**(6), 1182–1199 (2012).
27. X. Wei, A. Camino, S. Pi, T. T. Hormel, W. Cepurna, D. Huang, J. C. Morrison, and Y. Jia, "Real-time cross-sectional and en face OCT angiography guiding high-quality scan acquisition," *Opt. Lett.* **44**(6), 1431–1434 (2019).
28. Y. Jian, K. Wong, and M. Sarunic, "Graphics processing unit accelerated optical coherence tomography processing at megahertz axial scan rate and high resolution video rate volumetric rendering," *J. Biomed. Opt.* **18**(2), 026002 (2013).
29. J. Xu, K. Wong, Y. Jian, and M. Sarunic, "Real-time acquisition and display of flow contrast using speckle variance optical coherence tomography in a graphics processing unit," *J. Biomed. Opt.* **19**(2), 026001 (2014).

30. A. Camino, M. Zhang, S. S. Gao, T. S. Hwang, U. Sharma, D. J. Wilson, D. Huang, and Y. Jia, "Evaluation of artifact reduction in optical coherence tomography angiography with real-time tracking and motion correction technology," *Biomed. Opt. Express* **7**(10), 3905–3915 (2016).
31. Y. Chen, Y.-J. Hong, S. Makita, and Y. Yasuno, "Eye-motion-corrected optical coherence tomography angiography using Lissajous scanning," *Biomed. Opt. Express* **9**(3), 1111–1129 (2018).
32. M. J. Ju, M. Heisler, A. Athwal, M. V. Sarunic, and Y. Jian, "Effective bidirectional scanning pattern for optical coherence tomography angiography," *Biomed. Opt. Express* **9**(5), 2336–2350 (2018).
33. X. Wei, T. T. Hormel, S. Pi, Y. Guo, Y. Jian, and Y. Jia, "High dynamic range optical coherence tomography angiography (HDR-OCTA)," *Biomed. Opt. Express* **10**(7), 3560–3571 (2019).
34. S. B. Ploner, E. M. Moul, W. Choi, N. K. Waheed, B. Lee, E. A. Novais, E. D. Cole, B. Potsaid, L. Husvagt, J. Schottenhamml, A. Maier, P. J. Rosenfeld, J. S. Duker, J. Hornegger, and J. G. Fujimoto, "Toward quantitative optical coherence tomography angiography: visualizing blood flow speeds in ocular pathology using variable interscan time analysis," *Retina* **36**(Suppl 1), S118–S126 (2016).
35. K. Kurokawa, Z. Liu, and D. T. Miller, "Adaptive optics optical coherence tomography angiography for morphometric analysis of choriocapillaris [Invited]," *Biomed. Opt. Express* **8**(3), 1803–1822 (2017).
36. M. Salas, M. Augustin, L. Ginner, A. Kumar, B. Baumann, R. Leitgeb, W. Drexler, S. Prager, J. Hafner, U. Schmidt-Erfurth, and M. Pircher, "Visualization of micro-capillaries using optical coherence tomography angiography with and without adaptive optics," *Biomed. Opt. Express* **8**(1), 207–222 (2017).
37. K. Kurokawa, K. Sasaki, S. Makita, Y.-J. Hong, and Y. Yasuno, "Three-dimensional retinal and choroidal capillary imaging by power Doppler optical coherence angiography with adaptive optics," *Opt. Express* **20**(20), 22796–22812 (2012).
38. D. J. Wahl, R. Ng, M. J. Ju, Y. Jian, and M. V. Sarunic, "Sensorless adaptive optics multimodal en-face small animal retinal imaging," *Biomed. Opt. Express* **10**(1), 252–267 (2019).
39. J. Polans, D. Cunefare, E. Cole, B. Keller, P. S. Mettu, S. W. Cousins, M. J. Allingham, J. A. Izatt, and S. Farsiu, "Enhanced visualization of peripheral retinal vasculature with wavefront sensorless adaptive optics optical coherence tomography angiography in diabetic patients," *Opt. Lett.* **42**(1), 17–20 (2017).
40. R. S. Weinhaus, J. M. Burke, F. C. Delori, and D. M. Snodderly, "Comparison of fluorescein angiography with microvascular anatomy of macaque retinas," *Exp. Eye Res.* **61**(1), 1–16 (1995).
41. D. M. Snodderly, R. S. Weinhaus, and J. C. Choi, "Neural-vascular relationships in central retina of macaque monkeys (*Macaca fascicularis*)," *J. Neurosci.* **12**(4), 1169–1193 (1992).
42. A. Camino, R. Ng, J. Huang, Y. Guo, S. Ni, Y. Jia, D. Huang, and Y. Jian, "Depth-resolved optimization of real-time sensorless adaptive optics optical coherence tomography," *Opt. Lett.* **45**(9), 2612–2615 (2020).
43. M. J. Ju, M. Heisler, D. Wahl, Y. Jian, and M. Sarunic, "Multiscale sensorless adaptive optics OCT angiography system for in vivo human retinal imaging," *J. Biomed. Opt.* **22**(12), 1–12 (2017).
44. S. S. Gao, G. Liu, D. Huang, and Y. Jia, "Optimization of the split-spectrum amplitude-decorrelation angiography algorithm on a spectral optical coherence tomography system," *Opt. Lett.* **40**(10), 2305–2308 (2015).
45. J. P. Campbell, M. Zhang, T. S. Hwang, S. T. Bailey, D. J. Wilson, Y. Jia, and D. Huang, "Detailed Vascular Anatomy of the Human Retina by Projection-Resolved Optical Coherence Tomography Angiography," *Sci. Rep.* **7**(1), 42201 (2017).
46. W. Janponsri, J. Huang, R. Ng, D. J. Wahl, M. V. Sarunic, and Y. Jian, "Pseudo-real-time retinal layer segmentation for high-resolution adaptive optics optical coherence tomography," Arxiv preprint arXiv:2004.05264 (2020).
47. M. Guizar-Sicairos, S. T. Thurman, and J. R. Fienup, "Efficient subpixel image registration algorithms," *Opt. Lett.* **33**(2), 156–158 (2008).
48. M. F. Kraus, B. Potsaid, M. A. Mayer, R. Bock, B. Baumann, J. J. Liu, J. Hornegger, and J. G. Fujimoto, "Motion correction in optical coherence tomography volumes on a per A-scan basis using orthogonal scan patterns," *Biomed. Opt. Express* **3**(6), 1182–1199 (2012).
49. P. Zang, G. Liu, M. Zhang, C. Dongye, J. Wang, A. D. Pechauer, T. S. Hwang, D. J. Wilson, D. Huang, D. Li, and Y. Jia, "Automated motion correction using parallel-strip registration for wide-field en face OCT angiogram," *Biomed. Opt. Express* **7**(7), 2823–2836 (2016).
50. M. Heisler, S. Lee, Z. Mammo, Y. Jian, M. J. Ju, A. Merkur, E. Navajas, C. Balaratnasingam, M. F. Beg, and M. Sarunic, "Strip-based registration of serially acquired optical coherence tomography angiography," *J. Biomed. Opt.* **22**(3), 036007 (2017).
51. A. Camino, M. Zhang, L. Liu, J. Wang, Y. Jia, and D. Huang, "Enhanced quantification of retinal perfusion by improved discrimination of blood flow from bulk motion signal in OCTA," *Trans. Vis. Sci. Tech.* **7**(6), 20 (2018).
52. M. Reddikumar, A. Tanabe, N. Hashimoto, and B. Cense, "Optical coherence tomography with a 2.8-mm beam diameter and sensorless defocus and astigmatism correction," *J. Biomed. Opt.* **22**(2), 026005 (2017).
53. Q. Bo, Q. Yan, M. Shen, M. Song, M. Sun, Y. Yu, P. J. Rosenfeld, F. Wang, and X. Sun, "Appearance of polypoidal lesions in patients with polypoidal choroidal vasculopathy using swept-source optical coherence tomographic angiography," *JAMA Ophthalmol.* **137**(6), 642–650 (2019).
54. "Early treatment diabetic retinopathy study design and baseline patient characteristics: ETDRS Report Number 7," *Ophthalmology* **98**, 741–756 (1991).
55. "Early photocoagulation for diabetic retinopathy: ETDRS Report Number 9," *Ophthalmology* **98**(5), 766–785 (1991).

56. S. M. McClintic, S. Gao, J. Wang, A. Hagag, A. K. Lauer, C. J. Flaxel, K. Bhavsar, T. S. Hwang, D. Huang, Y. Jia, and S. T. Bailey, "Quantitative evaluation of choroidal neovascularization under pro re nata anti-vascular endothelial growth factor therapy with OCT angiography," *Ophthalmol. Retina* **2**(9), 931–941 (2018).